

Data Analysis Techniques for Microwave Imaging Reflectometry

Z.B. SHI, Y. NAGAYAMA¹), S. YAMAGUCHI¹), Y. HAMADA¹) and Y. HIRANO²)

The Graduate University for Advanced Studies, Toki 509-5292, Japan

¹*National Institute for Fusion Science, Toki 509-5292, Japan*

²*National Institute of Advanced Industrial Science and Technology, Tsukuba 305-8568, Japan*

(Received 11 December 2007 / Accepted 14 March 2008)

A data analysis technique for microwave imaging reflectometry (MIR) in the Large Helical Devices (LHD) and TPE-RX plasmas has been investigated. In LHD, the fast Fourier transform (FFT) is employed. The statistical properties of the fluctuation spectra on MIR signals are quantified by the time-frequency analysis by the ensemble average technique. Statistical analyses using cross-correlation and coherence spectra reveal the characteristics of MHD modes, such as wave numbers, mode numbers, and phase velocity. In TPE-RX, the wavelet analysis is more useful because the phenomena are transient in TPE-RX plasma.

© 2008 The Japan Society of Plasma Science and Nuclear Fusion Research

Keywords: density fluctuation, microwave imaging reflectometry, ensemble average, wavelet, FFT.

DOI: 10.1585/pfr.3.S1045

1. Introduction

Turbulence and instabilities have been considered to correlate with the properties of confinement, and thus, the spatial structure of the fluctuation continues to be the basic issue in the fluctuation study. Microwave imaging reflectometry (MIR) has been applied to the Large Helical Device (LHD) and TPE-RX [1, 2]. This technology is based upon the reflection of microwaves at the density-dependent cutoff layer, and the fluctuating phase of the reflected wave is dominated by the density fluctuation close to the cutoff layer. The reflecting signal has rich physics phenomena, which include the plasma turbulence and MHD instabilities [1–5].

Fluctuation signals often submerge in the strong background noises, such as electronic noise and thermal noise, especially when the reflection surface is in the core plasma region. After the onset of the turbulence, the spectrum becomes broad. The large-scale turbulence eddy may cause distortion of the spectrum. Therefore, observations are difficult from the oscillation even in the frequency domain.

Many digital noise reduction methods have been developed in previous studies [6–8]. These methods use statistical features of random noises, whose power spectral density is similar in all frequency bands. The expected error rate of the ensemble average decreases monotonically as a function of the number of the data sets in the ensemble average. Therefore, the statistical analysis of a fluctuating quantity over a long period of time may be useful to pickup fluctuating signals.

The short-time Fourier transform can show the time evolution of the fluctuation spectrum. The frequency resolution becomes worse at high-time resolutions. Therefore, it is difficult to obtain the time evolution of the rapid chang-

ing mode by short-time Fourier analysis. On the other hand, the wavelet transform is one of the most useful methods for the fluctuation analysis. It can analyze the time series that contains non-stationary frequencies or multi-scale structures by revealing the similar structures in the correlation.

This study presents the quantifying methods for the statistical properties of the fluctuation spectra based on MIR signals. Section 2 introduces the experiments in LHD. The FFT analysis method and the effects of ensemble average on the noise reduction in the spectrum are presented in Section 3. In Section 4, the cross-correlation analysis is applied to MIR data in LHD. Wavelet analysis is used to the TPE-RX plasma in Section 5. Significant results are as follows: the FFT spectrum with the ensemble average technique has been analyzed quantitatively to reduce the noise; this technique reveals three types of modes during high-power neutral beam injection (NBI) heating in LHD; the wavelet analysis shows higher time and frequency resolutions, and small structures are observed.

2. Experiment in LHD

Present MIR system on LHD has three antennas that separate in the toroidal and poloidal directions. A probe beam with frequencies of 53, 66, and 69 GHz in either the O- or the X-mode illuminates the plasma [1, 2]. The illuminating beam is parallel to the 20 cm diameter in the plasma, which is limited by the window of LHD. The receiving focus spot size in the plasma is about 3–4 cm in diameter. The beam separation is about 8.4–10 cm in the toroidal direction and 10–12 cm in the poloidal direction on the cutoff surface. Therefore, there is no overlapping between neighboring channels. The injection paths of the beams are optimized, which is in agreement with the ray

author's e-mail: shi.zhongbing@nifs.ac.jp

tracing simulation. The fluctuation signals are measured by the heterodyne receivers with a sampling frequency of 1 MHz. As an example of data analysis, we present an analysis of one shot (75414). This plasma has a toroidal magnetic field of 1.5 T and a major radius of 3.6 m, and is heated by the co-injected NBI with power of 2.5 MW and counter-injected NBI with power of 1 MW between $t = 0.3$ and 2.3 s. The ECH with the total power of 1.2 MW is injected between $t = 1.4$ and 2.0 s. The plasma beta is about 0.75% between $t = 0.9$ and 2.3 s. Since X-mode is used in MIR, the cutoff surface is determined by both the toroidal magnetic field and the electron density.

The density profile is obtained from the Thomson scattering by calibration using a microwave interferometer, of which the chord is equivalent to the laser beam of the Thomson scattering. The density profile is distorted due to misalignment of the laser beam. Also, the plasma center is shifted outward due to the Shafranov shift. Figure 1 shows the calibration of the density profile at 1.6 s. The red closed circles indicate the experimental data. The temperature has a peaked profile, but the density profile is strongly deformed and shows a declining trend, which is caused by the misalignment of the laser beam.

To recover the density profile, we assume that the density and temperature are uniform on a same magnetic surface. Firstly, polynomial fittings are used for the temperature and density profiles,

$$\begin{aligned} T_{e_fit}(R) &= \sum_{n=0}^N a_n R^n, \\ n_{e_fit}(R) &= \sum_{n=0}^N b_n R^n, \end{aligned} \quad (1)$$

where R is the radius, and a_n and b_n are the fitting coefficients. We use $N = 4$ for the temperature fitting and $N = 8$ for the density fitting. Before fitting, the data that are greatly apart from other data are removed. The plasma center (R_0) is determined from the temperature profile. Secondly, we assume that the $n_{e_fit}(R)$ includes a linear trend since $n_{e_fit}(R) = n_{e_cali}(R)(1 + c(R - R_0))$. Therefore, the density profile can be corrected as

$$n_{e_cali}(R) = n_{e_fit}(R)/(c(R - R_0) + 1), \quad (2)$$

where c is the slope of the linear fitting of the density profile. The density profile becomes quasi-symmetric (the blue solid line shown in Fig. 1(b)). Then, the density profile is adjusted by averaging the density $n_{e_cali}(R)$ at the same temperature surface. Finally, the absolute density profile (black solid line shown in Fig. 1(c)) is calibrated, as the line-integrated density equals to the microwave interferometer density. Figure 1(e) shows the normalized density and temperature profiles, which can be used to check the quality of the density reconstruction.

The cutoff frequency is obtained by calculating the plasma density and the toroidal magnetic field. Then the cutoff surface can be determined. As shown in Fig. 1(d),

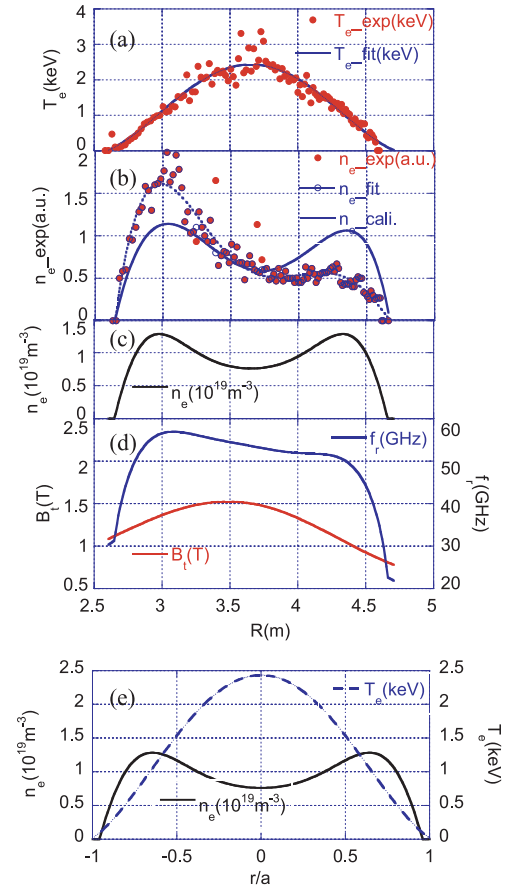


Fig. 1 Calibration of the reflection layer by Thomson data, (a) electron temperature profile, (b) electron density profile (before and after calibration), (c) the electron density profile after calibrated by microwave interferometer, (d) the toroidal magnetic field (B_t) and the X-mode cutoff frequency (f_i). (e) The normalized density and temperature profiles. The red dots are experimental data. The large discrete peaks are removed before fitting.

the cutoff layer of 53 GHz is close to the plasma axis; however, for the layers of 66 and 69 GHz, there are no cutoff layers, and the detectors receive interferential signals. We only analyze the reflection signals of 53 GHz illumination below. The plasma density is almost equal, and the cutoff layer of 53 GHz varies from 3.75 to 4.0 m (the normalized radius is about 0.15-0.4 m) between $t = 0.9$ and 2.3 s. Therefore, the curvature radius of the cutoff surface (≥ 15 cm) is larger than the illuminating beam radius (10 cm). The imaging of the fluctuation at the cutoff surface can be obtained using the MIR system.

3. FFT Analysis with the Ensemble Average

The frequency spectrum and the phase are obtained by Fourier analysis. The Fourier transformation $X(\omega)$ of the

signal $x(t)$ is given by

$$X(\omega, t) = \int_{t-\Delta t}^{t+\Delta t} w(t')x(t')e^{-j\omega t'} dt', \quad (3)$$

where $w(t)$ is the Hanning window function, which is used to reduce the leakage of the sideband. The short-time FFT analysis is used to show the time evolution of the spectrum.

In many situations, the signal from the plasma contains random noise. Sometimes its amplitude in the frequency domain is higher than the signal that we are interested in, and it masks the useful information. By the ensemble average technique in the frequency domain, the amplitude of the random fluctuations has an average power level in all frequency ranges. The ensemble average has less influence on the mode whose amplitude does not change in the ensemble time. Using a test parameter composed of a sinusoid and a random function, the qualitative effect of the noise on the signal in the frequency spectrum is shown.

The definitions of the signal-to-noise (S/N) ratio in the time and frequency domains are illustrated in Fig. 2(a) and (b), respectively. They are defined as the amplitude ratio between the test signal and random noise. Figure 2(c) shows the ratio between the absolute amplitude of the Fourier component at the frequency of the test signal and the amplitude of the noise in the frequency domain versus the S/N ratio in the time domain. Therefore, the y-axis can be called as the S/N ratio in frequency domain. The FFT time window is set as 2 ms. Here, the black solid line denotes the ratio without average, and the others are that with different ensemble numbers. The S/N ratio in the frequency domain increases with the ensemble number. A larger ensemble number is suggested for lower S/N signal. Figure 2(d) shows the relative ratio between the S/N signal in the frequency domain and the S/N signal in the time domain versus the ensemble number. The ratio changes greatly with the time window, but not with the signal frequency. The time window reflects the frequency broadening. It implies that the frequency broadening affects the present S/N. The ratio decreases with the frequency width. It becomes saturated as the ensemble number increases. Therefore, the improvement by the ensemble average on the noise reduction becomes weak at a larger ensemble number. The saturated threshold of the ensemble average with a long time window is smaller than that with a short time window. If the S/N ratio is lower than 1%, it is difficult to obtain the signal, even with a large ensemble number.

We assume 1.5 as the discriminating level of the FFT spectrum; in other words, the FFT amplitude of the signal is 1.5 times higher than the maximum amplitude of the noise in the frequency domain. By the ensemble average technique, the value is about 0.03, while it is about 0.1 without the ensemble average using a 2 ms time window. The distinguishable value mainly depends on the frequency broadening, and not on the signal frequency. This

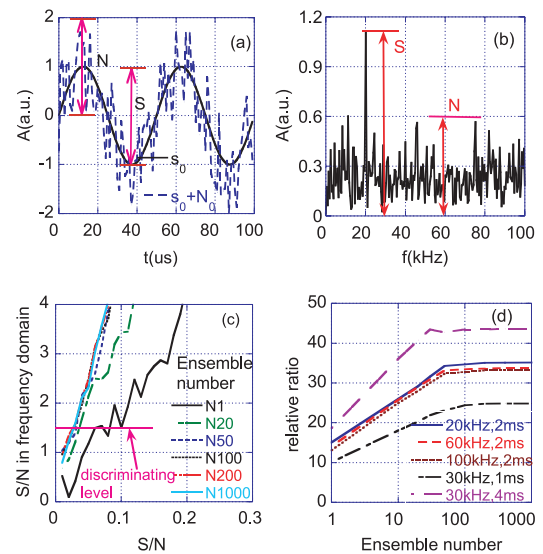


Fig. 2 Effects of S/N on the FFT spectrum. (a) definition of S/N in time domain ($S/N = 1$ case), (b) definition of S/N in frequency domain ($S/N = 0.1$ case), (c) the S/N in frequency domain versus S/N ratio in time domain, here, the y-axis is the ratio between the FFT amplitude of the test signal and the maximum amplitude of background fluctuation in frequency domain; (d) The relative ratio between S/N in frequency domain and S/N in time domain as a function of ensemble numbers. The signals with different frequency show similar ratio at 2 ms time window. The relative ratios with 1 ms and 4 ms time window are also plotted.

simulation only shows the qualitative effect of the noise on the signal. For the quantitative estimation, the frequency broadening should be considered. In conclusion, the ensemble technique is an effective way to reduce noise. This method requires that the lifetime of the mode be longer than the time window of the FFT. If not, the signal might be distorted by the averaging and the new analysis method that has both high-time and high-frequency ability, should be used, e.g., wavelet transforms [9, 10].

As an example of FFT analysis by the ensemble average technique for analyzing the MIR signals is shown in Fig. 3, which shows the power spectrum with/without the ensemble average at 1.6 s. Here, the 4-ms time window is used for the power spectrum without the average, and 50 FFT windows with the time scale of 2 ms each are used for the power spectrum with the ensemble average. Without the ensemble average, the MHD modes are concealed in the strong background fluctuations. The fluctuation is reduced with the ensemble average. If all the fluctuation components represent white noise, the fluctuations should be reduced to 0.14, such as the fluctuations at 60-80 kHz and 30-50 kHz. The average has less impact on the mode frequency. With the ensemble average, the fluctuation of the power is reduced significantly, and the MHD modes clearly appear.

Figure 4 shows the contour plot of the time evolution

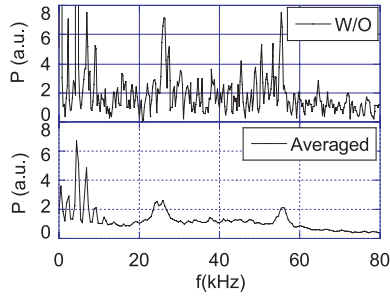


Fig. 3 Power spectrum at 1.6 s (Top: without average and 4 ms time window is used. Bottom: with ensemble average, 50 data sections with the time scale of 2 ms each are used.)

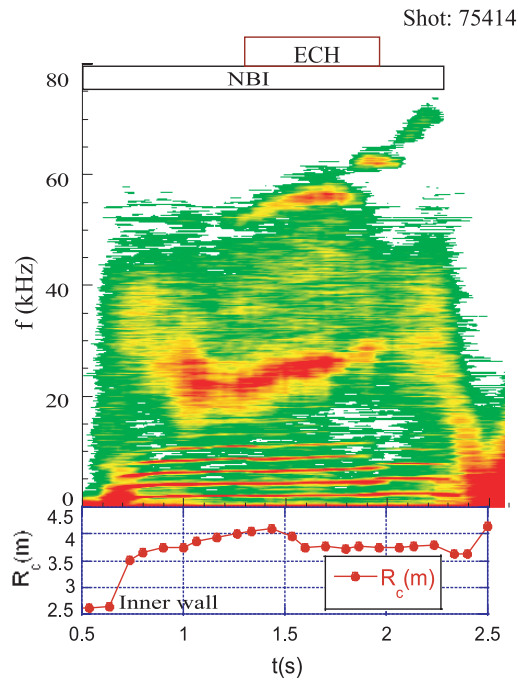


Fig. 4 Time-frequency plot of FFT spectrum, the bottom is the cutoff position.

of the frequency spectrum and the cutoff radius. Three types of fluctuations appear in the MIR signals. In the low-frequency range, the density fluctuation has a fundamental frequency of 2.3 kHz and its higher harmonics. It appears at 0.7 s when observing the cutoff surface, and disappears after turning off the NBI power. The cutoff surface varies from 3.75 to 4.0 m between $t = 0.8$ and 2.3 s. It seems that the onset of this mode depends on the power of the neutral beam, and the frequency of this mode relates to the ion temperature [11]. At $t = 0.9$ s, a mid-frequency mode (~ 23 kHz) with a wide profile appears when the plasma temperature increase to flat top. When turning on the ECH power, this frequency increases to 26 kHz, and it disappears after turning off the ECH power. When turning on the ECH power, a high-frequency mode (~ 55 kHz) appears. This is in the range of the Alfvén frequency. The mode frequency increases with time, and it is up to 70 kHz at

$t = 2.2$ s. This mode exists after turning off the ECH power, indicating that this mode may be related to the energetic ion mode, but it is induced by the energetic electrons.

4. Cross-Correlation Analysis

The cross-power spectral analysis is used to identify the two time series that have similar spectral properties. The cross-power spectrum between the two time series $x(t)$ and $y(t)$ is defined as

$$G_{xy}(\omega) = Y(\omega)X(\omega)^*, \quad (4)$$

where the asterisk (*) denotes the complex conjugate. $X(\omega)$ and $Y(\omega)$ are the discrete Fourier transforms of the time series $x(t)$ and $y(t)$, respectively. The phase shift between the two time series is given by

$$\Phi_{xy}(\omega) = \tan^{-1} \left\{ \frac{\text{Im} [G_{xy}(\omega)]}{\text{Re} [G_{xy}(\omega)]} \right\}. \quad (5)$$

In order to obtain the phase shift whose value corresponds to a high correlation in the frequency domain, the coherence spectrum is introduced, and it is defined by the cross-power spectrum normalized by the total power as

$$\gamma_{xy}(\omega) = \frac{|\langle G_{xy}(\omega) \rangle|}{\sqrt{\langle G_{xx}(\omega) \rangle \langle G_{yy}(\omega) \rangle}}, \quad (6)$$

where the bracket ($\langle \rangle$) denotes ensemble average. The coherency is bounded between 0 and 1, and the high value corresponds to high correlation, and zero represents completely uncorrelated. The statistical confident level of the coherence spectrum is determined by the number of the independent time series ($1/\sqrt{N}$).

The phase-frequency spectrum shows the dispersion relations of the MHD mode and turbulence with a distinct phase shift and propagation direction in a two-dimensional plot. It can be obtained by the two-point cross-correlation method,

$$S(\Phi, \omega) = \langle |G_{xy}(\omega)| \delta(\Phi_{xy}(\omega) - \Phi) \rangle. \quad (7)$$

In the calculation, the delta function is replaced by a rectangular window. The width of the window depends on the number of the discrete sections in the value range of $\Phi_{xy}(\omega)$. The phase velocity and the mode number can be obtained from the distance between two detecting points of the wave number. Substituting the phase shift for the wave number in Eq. (7), the wave number frequency spectrum [7] can be obtained.

Figure 5 shows the cross-power spectrum, coherence, and phase shift by the ensemble average method. Note that when calculating the cross-power and the coherence spectra, FFT is performed at every 200 data sections with the time period of 4 ms each. The overlap between the neighboring sections is half of the time window. Before calculating the spectrum, the mean value and the linear trend have

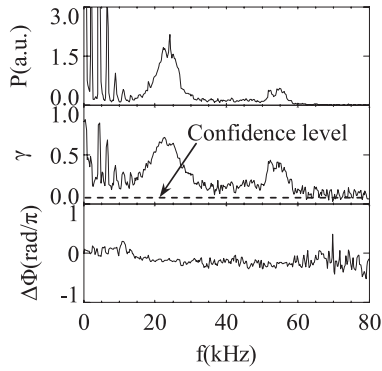


Fig. 5 Cross-power spectrum, coherence and phase shift in the poloidal direction at $t = 1.6$ s.

been removed from every time series. When the mode appears, the cross-power spectrum is peaked, and coherence becomes high. The phase shift versus frequency shows smaller jumps.

Figure 6(a) and (c) shows the contour plots of the phase-frequency spectra, $\log(S(\Phi, \omega))$, in the poloidal and toroidal directions at $t = 1.5$ s, respectively. The highlight color corresponds to the large amplitude. When the mode appears, the phase shift has a peaked profile. Note that the phase shift has a broad profile, especially in the low-frequency mode. One possible reason is that the strong effects of the turbulence may cause the distorted distribution of the spectrum. Another reason might be the noise. The width of the phase shift profile slightly decreases with increasing independent time events, and becomes constant at large time events. In this analysis, the independent events are sufficient for the ensemble average, although the lifetime of the mode is not very long. Even so, the phase shift can be obtained from the fitting profile of the phase spectrum.

The phase shift at the peak of the fitting profile is close to the ensemble phase shift $\langle \Phi_{xy}(\omega) \rangle$. As shown in Fig. 6(b), the poloidal phase shift is about 0.05π at $f = 4.4$ kHz. It is the same as the phase shift in Fig. 5. Therefore, the poloidal wave-number and mode number are $k = 1.5 \text{ m}^{-1}$ and $m \sim 1$, respectively. The toroidal phase shift is about 0.07π at $f = 4.4$ kHz. The toroidal wave number and mode number are $k = 2.6 \text{ m}^{-1}$ and $n \sim 9$, respectively. The mode numbers of the 26 and 56 kHz are $m = 2/n = 20$, $m/n = 3/26$, respectively. Assuming that the half width at half maximum (HWHM) of the fitting curve is the phase error, the errors of the poloidal mode numbers are about 1. The errors of the toroidal mode numbers are about 20. The phase shift has a linear trend, and the average phase velocity ω/k is about 15 km/s.

The noise distorts not only the power spectrum but also the phase spectrum. When the signal is too weak, the average phase spectrum $\langle \Phi_{xy}(\omega) \rangle$ largely fluctuates, as seen between 60 and 80 kHz in Fig. 5. In Fig. 6 (a) and (c), the phase shift spectrum has a broad profile. The phase

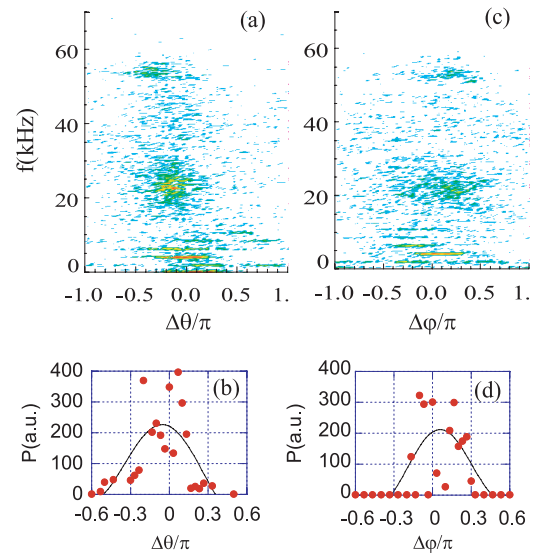


Fig. 6 (a) The phase-frequency spectrum, $\log(S(\theta, f))$, in poloidal direction at $t = 1.5$ s, (b) The fitting of the poloidal phase shift at $f = 4.4$ kHz, (c) The phase-frequency spectrum, $\log(S(\varphi, f))$, in toroidal direction at $t = 1.5$ s, (d) The fitting of the toroidal phase shift at $f = 4.4$ kHz

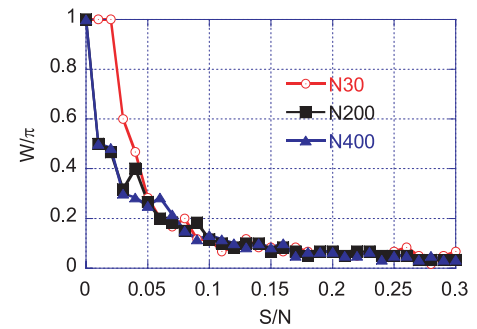


Fig. 7 The half width of the phase profile with different ensemble numbers versus S/N ratio in the phase frequency spectrum

shift at the peak of the fitting curve is the average phase shift. The noise level of the raw signal can be estimated from the width of the phase shift. Here, the width of the phase shift profile is defined as the half width over 10% maximum in the phase shift spectrum.

Figure 7 shows the width of the phase shift versus the S/N ratio. The width decreases rapidly as the S/N ratio increases. It shows the same width if the S/N ratio is larger than 0.05. The average over a few ensemble numbers at small S/N ratio shows a broadening profile. The width becomes constant by averaging over the large ensemble numbers, for example, the ensemble average numbers $N = 200$ and $N = 400$. In other words, when the ensemble average number is large enough, the width mainly depends on the S/N ratio, not on the ensemble average number. It is consistent with the results shown in Fig. 2. The ensemble number $N = 200$, shown by the solid line with black

square, is used in the calculation in Fig. 6. The noise level of the raw signal is estimated from the width of the phase shift. Comparing the simulation and the phase shift shown in Figs. 6(b) and (d), the S/N of MIR raw signal is about 0.05.

5. Wavelet Analysis of MIR Signals

5.1 Experiment in TPE-RX

The MIR diagnostic has been used for the density fluctuation measurement on the large reverse field pinch (RFP) device, TPE-RX ($R = 1.72$ m, $a = 0.45$ m) [14]. The 2D image of the local density fluctuation has been obtained using a 2×2 antenna array with a temporal resolution of $1 \mu\text{s}$ and a spatial resolution of 3.7 cm. The probe beam with a frequency of 20 GHz in the O-mode illuminates the plasma, so that the cutoff density is $0.5 \times 10^{19} \text{ m}^{-3}$. The density is measured using a dual-chord interferometer. One chord passes through the plasma center and the other passes through the normalized radius $r/a = 0.69$. The density profile is obtained by fitting the experimental data with the profile function $n_e(r, t) = n_e(0, t)(1 - r^4)(1 + C(t)r^4)$. Here, the profile factor $C > 1$ represents the hollow density, and $C < 1$ is the peaked density profile. In this paper, we analyze a pulsed poloidal current drive (PPCD) plasma. In this case, the normalized cutoff radius is about 0.8-0.9 m. This region is close to the reverse field surface, and the fluctuation changes rapidly [14, 15].

5.2 Wavelet analysis

The wavelet transform of time series is its integration with the local basis functions, i.e. wavelet functions, which can be stretched and translated with flexible resolution in both time and frequency.

$$W(s, t) = \frac{1}{\sqrt{s}} \int_{T-\Delta t}^{T+\Delta t} x(t') \psi^* \left(\frac{t' - t}{s} \right) dt, \quad (8)$$

where s is the scale parameter, t is the time translation parameter, the asterisk(*) denotes the complex conjugate, and $\psi(t)$ is the wavelet function. We use the Morlet wavelet function because it has a good balance between the time and frequency localization. Furthermore, the Morlet wavelet analysis preserves phase information that is very important for the fluctuation analysis. The Morlet wavelet waveform is a sinusoid with a Gaussian envelope, defined as

$$\psi(s, t) = \sqrt{s} \exp \left[i\omega_0 \left(\frac{t' - t}{s} \right) - \frac{1}{2} \left(\frac{t' - t}{sd} \right)^2 \right], \quad (9)$$

where ω_0 is the dimensionless frequency, t' is the dimensionless time, and d is a constant related to the Gaussian envelope. As d decreases, the time resolution improves, whereas the frequency resolution becomes worse. As d increases, the Morlet wavelet reaches the Fourier transform. Here we take $d = 1$ and $\omega_0 = 2\pi$. The scale is the inverse of the frequency, thus $s = 1/f$ [9].

The calculations of Wavelet transform can be done as a convolution, which is considerably faster in the frequency domain,

$$W(s, t) = \hat{F}^{-1} [X(\omega)\Psi(\omega)], \quad (10)$$

where X and Ψ are the Fourier transforms of the time series $x(t)$ and Morlet wavelet, respectively, and \hat{F}^{-1} is the inverse Fourier transform. Based on the same concepts in the previous section, the cross-wavelet spectrum, phase shift, and wavelet coherence can be obtained [9, 13].

5.3 Wavelet analysis of MIR data in TPE-RX

The FFT spectrum is the integrated transform within the FFT time. It is difficult to distinguish the mode, which changes in FFT time. If we decrease the time window, the frequency resolution becomes worse. Wavelet analysis can reveal the fluctuation structure at any scale in correlation with a high-time resolution. This is advantageous to analyze the fluctuation of the RFP plasma. To further understand the difference between the FFT and wavelet analysis, the toroidal cross-power spectra (shot: 52973, a PPCD plasma, cut off layer: $r/a = 0.9$) by FFT and wavelet transforms are compared in Fig. 8. Before analyzing, a band pass filter with a frequency range 5-50 kHz is used. The time window of FFT is 0.25 ms and the frequency resolution is 4 kHz. Therefore, it is difficult to get the mode,

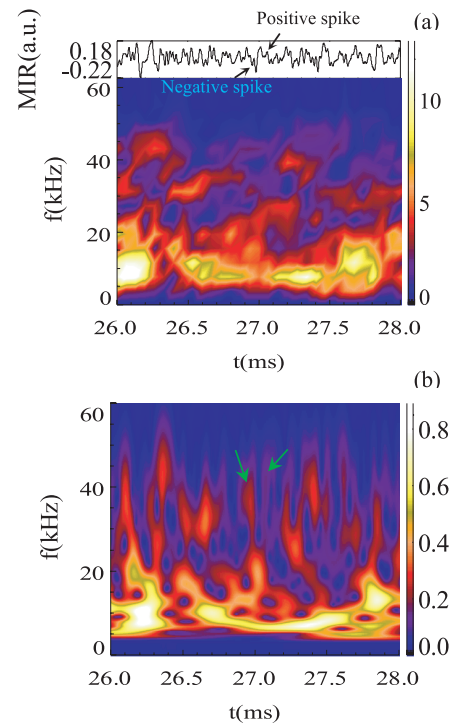


Fig. 8 (a) Contour plot of the toroidal cross-power spectrum $G_{xy}(\omega, t)$ (FFT time window: 0.25 ms) and MIR signal (Shot: 52973, Cut off layer: $r/a = 0.9$), (b) Toroidal cross-wavelet spectrum $|W_a(s, t)W_b^*(s, t)|$. The MIR signal at the top is filtered by a band pass filter (5-50 kHz).

which changes faster than 250 μs . However, in the wavelet spectrum, the time duration of the structure is about 100 μs . The high-frequency mode shows a shorter duration.

Fourier transform has a fixed resolution. We cannot distinguish the frequency, which changes within the FFT time. The spectrum may be transverse elongated by the integration in the range of the time window. For example, the fluctuation between 30-35 kHz from 26.4 to 26.7 ms is changing both in frequency and amplitude, but it has the same frequency and amplitude in FFT. Comparing the FFT and wavelet spectra between 26.5 and 27.6 ms, the frequency evolution between 7-10 kHz in the FFT is less clear than that in the wavelet analysis. Therefore, wavelet transform can give good time resolution for high-frequency events and good frequency resolution for low-frequency events. It is sensitive to the transient fluctuation.

Since the Morlet wavelet waveform is sinusoid with Gaussian envelope, it may fail in tracking the very sharp pulses. In this case, the complex Paul wavelet function can be used [13]. On the other hand, the Morlet wavelet may fail in tracking the high-frequency components due to the low-frequency components. This problem can be solved by changing the time and frequency resolutions (adjusting the parameter d in Equation (9)), or using a high-pass filter.

6. Summary

In summary, the analysis of plasma density fluctuation on LHD and TPE-RX has been performed based on MIR signals. The ensemble technique has been developed to reduce the noise effect in the spectrum analysis. By this technique, the statistical property of the fluctuation is obtained more accurately than single data. The width of the phase profile in the phase-frequency spectrum becomes wider as

the ratio of S/N in MIR raw signal is worse. MHD modes are observed during high-power NBI and ECH heating. The mode numbers are obtained by the cross-correlation technique. The wavelet analysis shows higher time and frequency resolutions, and the evolution of small structures is observed.

Acknowledgments

This study is supported by National Institute of Natural Sciences (NIFS07KEIN0021) and by National Institute for Fusion Science (NIFS07ULPP525).

- [1] S. Yamaguchi *et al.*, *Rev. Sci. Instrum.* **77**, 10E930 (2006).
- [2] Y. Nagayama, S. Yamaguchi, Z.B. Shi *et al.*, *Proceedings of ITC/ISHW2007*, P1-080.
- [3] R. Sabot *et al.*, *Plasma Phys. Control. Fusion* **48**, B421 (2006).
- [4] H. Park *et al.*, *Rev. Sci. Instrum.* **74**, 4239 (2003).
- [5] E. Mazzucato, *Rev. Sci. Instrum.* **69**, 2201 (1998).
- [6] E.B. Hooper, *Plasma Physics* **13**, 1 (1971).
- [7] Ch. P. Ritz *et al.*, *Rev. Sci. Instrum.* **59**, 1739 (1988).
- [8] G.S. Xu *et al.*, *Physics of Plasmas* **13**, 102509 (2006).
- [9] A. Grinsted, J.C. Moore and S. Jevrejeva, *Nonlinear Processes in Geophysics* **11**, 561 (2004).
- [10] V.P. Budaev, I.M. Pankratov, S. Takamura *et al.*, *Nucl. Fusion* **46**, S175 (2006).
- [11] S. Yamaguchi, Y. Nagayama, Z.B. Shi *et al.*, *Proceedings of ITC/ISHW2007*, P1-082.
- [12] T. Kass, H.S. Bosch, F. Hoenen *et al.*, *Nucl. Fusion* **38**, 807 (1998).
- [13] Christopher Torrence and Gilbert P. Compo, *Bulletin of the American Meteorological Society* **79**, 61 (1998).
- [14] Y. Hinaro, Y. Maejima, T. Shimada *et al.*, *Nucl. Fusion* **36**, 721 (1996).
- [15] P.R. Brunzell, Y. Maejima, Y. Yagi *et al.*, *Phys. Plasmas* **1**, 2297 (1994).